On the b-value Dependency of Injection-Induced Seismicity on Geomechanical Parameters

Yusuke mukuhira[1], Takatoshi Ito[1], Michael Fehler[2], Elvar K Bjarkason[1], Hiroshi Asanuma[3], and Markus O. Häring[4]

[1]Tohoku University
[2]MIT
[3]National Institute of Advanced Industrial Science and Technology (AIST)
[4]Häring Geo-Project

November 21, 2022

Abstract

Variability in the b-value, which describes the frequency distribution of earthquake magnitudes, is usually attributed to variations in differential stress in the setting of natural and laboratory earthquakes. However, differential stress is unlikely to explain b-value variations on the reservoir scale of injection-induced seismicity cases where significant differential stress variability can hardly be expected. We investigate the responsible geomechanical parameters for the b-value reduction observed in injection-induced seismicity at the Basel EGS field in Switzerland, for which a measured *in-situ* stress model and fault orientations of numerous microseismic events are available. We estimate the shear and normal stresses along faults, differential stress, pore pressure increase at failure, and the Coulomb failure stress, for each event. Event magnitude and shear stress display the most systematic and clear correlation between each other, while other parameters do not show a clear correlation with event magnitude. We further examine the relationship between the b-value and these geomechanical parameters. We discover that the b-value systematically decreases with increasing shear stress. Again, other geomechanical parameters do not show a clear correlation with the b-value. We conclude that b-value variability is explained by variations in shear stress in the injection-induced seismicity setting, where near constant differential stress conditions are expected. Furthermore, we observe that b-value reduction with time also correlates with an increasing number of events along faults having high shear stress, which strongly supports our conclusions. Thus, we discovered a profound physical mechanism behind b-value variation in injection-induced seismicity beyond general understandings of b-value variation.

Hosted file

`jgr2021muku_supporting-information_word.docx` available at https://authorea.com/users/526830/articles/596681-on-the-b-value-dependency-of-injection-induced-seismicity-on-geomechanical-parameters

Hosted file

`essoar.10507492.1.docx` available at https://authorea.com/users/526830/articles/596681-on-the-b-value-dependency-of-injection-induced-seismicity-on-geomechanical-parameters

On the *b*-value Dependency of Injection-Induced Seismicity on Geomechanical Parameters

Y. Mukuhira[1], T. Ito[1], M. C. Fehler[2], E. K. Bjarkason[1], H. Asanuma[3], and M. O. Häring[4]

[1]Institute of Fluid Science, Tohoku University, 2-1-1 Katahira, Aoba-ku, Sendai, Miyagi 980-8577, Japan.

[2]Earth Resources Laboratory, Department of Earth, Atmospheric and Planetary Sciences, Massachusetts Institute of Technology, Cambridge, Massachusetts, 02139, USA

[3]Fukushima Renewable Energy Institute, National Institute of Advanced Industrial Science and Technology (AIST), 2-2-9 Machiike-dai, Koriyama, Fukushima 963-0298, Japan.

[4]Geo Explorers Ltd., Wasserturmplatz 1, CH-4410, Liestal, Switzerland.

Corresponding author: Yusuke Mukuhira (mukuhira@tohoku.ac.jp)

Key Points:

- We investigate the *b*-value dependency on geomechanical parameters using *in-situ* stress information from borehole logging analysis
- The *b*-value systematically correlates with the shear stress rather than other geomechanical parameters
- We discovered a novel interpretation behind the *b*-value reduction in the injection-induced seismicity setting

Abstract

Variability in the *b*-value, which describes the frequency distribution of earthquake magnitudes, is usually attributed to variations in differential stress in the setting of natural and laboratory earthquakes. However, differential stress is unlikely to explain *b*-value variations on the reservoir scale of injection-induced seismicity cases where significant differential stress variability can hardly be expected. We investigate the responsible geomechanical parameters for the *b*-value reduction observed in injection-induced seismicity at the Basel EGS field in Switzerland, for which a measured *in-situ* stress model and fault orientations of numerous microseismic events are available. We estimate the shear and normal stresses along faults, differential stress, pore pressure increase at failure, and the Coulomb failure stress, for each event. Event magnitude and shear stress display the most systematic and clear correlation between each other, while other parameters do not show a clear correlation with event magnitude. We further examine the relationship between the *b*-value and these geomechanical parameters. We discover that the *b*-value systematically decreases with increasing shear stress. Again, other geomechanical parameters do not show a clear correlation with the *b*-value. We conclude that *b*-value variability is explained by variations in shear stress in the injection-induced seismicity setting, where near constant differential stress conditions are expected. Furthermore, we observe that *b*-value reduction with time also correlates with an increasing number of events along faults having high shear stress, which strongly supports our conclusions. Thus, we discovered a profound physical mechanism behind *b*-value variation in injection-induced seismicity beyond general understandings of *b*-value variation.

Plain Language Summary

For natural earthquakes and laboratory earthquakes, observed slope variability in the r frequency magnitude distribution (*b*-value) is commonly explained by variability in the applied stress. However, for injection-induced earthquakes that occur associated with fluid injection into the earth's subsurface, observed changes in the *b*-value cannot be well explained by variations in the earth's stress level. This is because the stress state is relatively constant over the narrow depth range targeted for subsurface development, and the physical processes that give rise to injection-induced seismicity are different to those of natural and laboratory earthquakes. We comprehensively investigate the relationship between the *b*-value and geomechanical parameters. We utilize directly measured stress information and combine it with seismological analysis results of the injection-induced seismicity observed in our study field. We found that variability in the *b*-value is better explained by shear stress, which quantifies the stress acting along the plane of a fracture that slips. The results indicate that, for injection-induced seismicity, shear stress explains the prevalence of different *b*-value better than any other geomechanical parameter, including earth's stress level and pore pressure. This observation may contribute in shaping operation protocols aimed at reducing the risk of large induced seismicity.

1 Introduction

One of the well known empirical laws in seismology is the Gutenberg-Richter (GR) law which states that earthquake magnitude size distribution follows a power law (Gutenberg & Richter, 1944). From the power law, the log of the expected number of earthquakes larger than magnitude M is given as $\log N = a - bM$, where a-value designates the total number of earthquakes of $M \geqq 0$ and the b-value defines the slope of the magnitude frequency distribution. Since the b-value indicates the relative ratio of the number of large and small earthquakes, the b-value is of interest for earthquake prediction and hazard analysis (e.g., Nanjo et al., 2012; Nanjo & Yoshida, 2018). In general, the b-value universally converges to 1 when considering large enough volumes (Kagan, 1999); however, b-value variation in time and space has been observed in several seismogenic regions (e.g., Wiemer & Wyss, 1997). The b-value reduction is often attributed to an increase in differential stress which was proposed based on several laboratory experiments (Scholz, 1968; Amitrano, 2003; Goebel et al., 2013). A number of subsequent studies have investigated physical mechanisms to explain b-value variability, namely variability in differential stress (e.g., Ide et al., 2016; Mori & Abercrombie, 1997; Nishikawa & Ide, 2014; Scholz, 2015; Schorlemmer et al., 2005). Additionally, b-value dependency on rake angles, and depth has been observed (Petruccelli, Gasperini, et al., 2019; Petruccelli, Schorlemmer, et al., 2019). Another study reconfirmed a dependency of b-value and the differential stress, which increases with depth using a representative stress gradient (Scholz, 2015). As in early work, where the b-value was considered to correlate with fracture strength (Scholz, 1968), the b-value also correlates with Coulomb Failure Stress (*CFS*) change, which is a relative form of strength (Gulia et al., 2018). Thus, b-value variation is attributed to the differential stress or a proxy of differential stress. However, comprehensive correlation has not yet been established between the *in-situ* stress in an earthquake region to the b-value; this is due to the technical difficulty of measuring *in-situ* stress at great depth.

Meanwhile, induced seismicity has been an important topic in seismology for the last decade as a result of the rapid increase of unconventional resource projects, which apply fluid injection to facilitate the extraction of resources from the subsurface. In that new topic in seismology, b-values are relevant when it comes to assessing the seismic hazard caused by injection (van der Elst et al., 2016; McGarr, 2014; Shapiro et al., 2010). Our study considers induced seismicity sequences observed at the Basel EGS (enhanced geothermal system) site, Switzerland, for which we can study induced seismicity in combination with reliably measured *in-situ* stress data. Many studies, some of which have considered b-value analysis, have contributed to the understanding of the seismicity at Basel (Bachmann et al., 2011a, 2012; Catalli et al., 2013; Goertz-Allmann et al., 2011; Mukuhira et al., 2013). Goertz-Allmann et al. (2011) estimated stress drop of seismic events at Basel and found that events near the injection well showed small stress drop and that events far from the injection well show large stress drop. They concluded that the lower stress drop near the injection well was due to a decrease in differential stress caused by pore pressure. Spatial and time dependent behavior of the b-value was observed for the same data-set where the b-value was high near the injection well and decreased away from the well (Bachmann et al., 2012). They linked the b-value reduction and differential stress assuming heterogeneous differential stress distribution.

We recently proposed another way to interpret the b-value reduction observed in the Basel data, where we reported a b-value dependency on shear stress for the injection induced seismicity case (Mukuhira et al., 2021a). We divided the seismic catalog based on different shear

stress threshold and estimated *b*-values for groups with values higher and lower than the threshold. We had following three key observations: 1) the *b*-value from the group having normalized shear stress (NSS) higher than the threshold, and 2) the *b*-value from the group having NSS lower than the threshold both show a dependency on the NSS thresholds, and 3) the *b*-value from the higher NNS group was always lower than that from the lower NNS group. These observations led to the conclusion of *b*-value dependency on NSS. In this study, fully utilizing *in-situ* stress measurements from borehole logging analysis, we comprehensively study the relationship between *b*-value variation and important geomechanical parameters, including shear stress, normal stresses on faults, differential stress, pore pressure increase, and *CFS*. To follow up on our previous study (Mukuhira et al., 2021a), we further investigate the *b*-value dependency on geomechanical parameters. Then we discuss the mechanism behind the *b*-value reduction observed in injection-induced seismicity beyond the simple *b*-value variation observation in time and space.

We start by reviewing the geomechanical theory for the injection-induced seismicity settings, natural earthquakes, and the laboratory experimental setting. We discuss the physical role of relevant geomechanical parameters and links to *b*-value variation. We present the field study area, Basel, including the microseismic and *in-situ* stress data. First, our analysis shows simple comparisons between event magnitude and geomechanical parameters. Then, the *b*-value dependency analysis results are presented. We discuss the *b*-value variation based on our analysis. We further discuss the consistency of our findings by comparing the conventional understanding or interpretation of *b*-value dependency and relevant studies.

2 Geomechanical Theory

2.1 Injection-Induced Seismicity Case

Shear slip on a fault initiates when the frictional strength of the fault yields to the shear stress on the fault. This process is widely described by the following Coulomb failure criterion:

$$\tau = \mu(\sigma_n - p) \tag{1}$$

where τ is the shear stress on the fault, μ is the friction coefficient, σ_n is the normal stress on the fault, and p is the pore pressure. In the situation of induced seismicity, p can be decomposed into a hydrostatic part p_{hyd} and a pore pressure increase part Δp such that $p = p_{hyd} + \Delta p$. An increase in pore pressure decreases the effective normal stress $\sigma_n - p$ and reduces the fault's frictional resistance, described by the right-hand side of equation (1), resulting in shear slip along the fault (Pine & Batchelor, 1984). If we consider a situation where we know the shear stress and normal stress, we can estimate the pore pressure increase required for shear failure using equation (1). Accordingly, the necessary pore pressure increase for shear slip is

$$\Delta p = \sigma_n - p_{hyd} - \frac{\tau}{\mu} \tag{2}$$

In the following discussions, Δp denotes the pore pressure increase required to trigger shear slip, as defined in equation (2). Thus, we can use seismic events to estimate pore pressure changes Δp

assuming an appropriate friction coefficient, the availability of stress information (stress magnitude and orientation) and fault orientation, since

$$\tau = \{a_1{}^2 a_2{}^2 (S_1 - S_2)^2 + a_2{}^2 a_3{}^2 (S_2 - S_3)^2 + a_3{}^2 a_1{}^2 (S_3 - S_1)^2\}^{\frac{1}{2}}, \quad (3)$$

$$\sigma_n = a_1{}^2 S_1 + a_2{}^2 S_2 + a_3{}^2 S_3, \quad (4)$$

where a_n (n=1, 2 ,3) are directional cosines for the principal stresses ($S_1 > S_2 > S_3$) relative to the vector normal to the fault plane. Conceptually, when it comes to injection-induced seismicity, Δp functions as the relative stress index to the failure since only the pore pressure increase controls the initiation of shear failure. Figure 1a depicts this situation.

Using Mohr's stress circle and a friction coefficient μ = 0.6, point 1 in Figure 1a shows the stress state of a well-oriented fault (a fault which slips with the minimum pore pressure increase). The horizontal coordinate of point 1 is the normal stress on a well-oriented fault σ_{n1} and the vertical coordinate of point 1 is the shear stress along the fault τ_1. For the initial hydrostatic state, the Coulomb failure criterion line of gradient 0.6 is outside the subcritical Mohr stress circle. With the increase of pore pressure due to injection, the failure line shifts to the right until it intersects point 1. Note that moving the failure line to the right is in principle the same as the explanation of a Mohr stress circle moving to the left (Zoback, 2007), because failure is discussed in terms of a relative distance between the failure line and the Mohr stress circle. In this case, the normal stress is specified along the horizontal axis as in (Kanamori & Brodsky, 2004). Point 2 shows a stress state of an arbitrary fault which has an orientation different than a well-oriented fault, so point 2 is within the Mohr circle. The shear stress (τ_2), normal stress (σ_{n2}), and pore pressure increase (Δp_2) for that fault have different values to those of the well-oriented fault. In particular, Δp_2 is larger than Δp_1. We further introduce point 3 showing the stress state of the fault having maximum shear stress. The strike of this fault has a 45 degree angle to the maximum stress direction. Point 3 is at the top of the Mohr circle. Note that Δp_2 and Δp_3 are equivalent though their shear and normal stresses are different.

In a natural earthquake setting, the relative stress index to the failure is often expressed as Coulomb failure stress (*CFS*), defined as (Harris, 1995; Beeler et al., 2000)

$$CFS = \tau - \mu(\sigma_n - p) \quad (5).$$

When *CFS* is positive, the failure criterion is satisfied, and the fault is critical. Conversely, a negative *CFS* indicates a fault below a critical condition.

In the injection-induced seismicity setting discussed above, when the shear stress and normal stress are constant, the pressure p is the only value that varies in equation (5). At the moment when pore pressure increase causes shear slip along a fault, equations (5) should be zero. When $p = p_{hyd}$ in equation (5), the change in Coulomb failure stress needed to induce shear failure is

$$CFS = \mu \times (-\Delta p) \quad (6)$$

The pore pressure change, Δp acts against the normal stress. Therefore, Δp is shown along the horizontal axis in the Mohr diagram (Figure 1a). Differently, *CFS* relates to shear stress and is, therefore, shown along the vertical axis in the Figure 1a, where *CFS* corresponds to the vertical distance from the point of the stress state to the failure line of the initial condition as CFS_i (i=1, 2, 3) shows in Figure 1b.

We see from equation (6) that Δp and *CFS* are almost identical in terms of relative stress index to the failure in theory. In the context of the injection-induced seismicity case, Δp is important since pore pressure increase is the main driver causing failure. For the natural earthquake setting, previous studies found that *b*-value is correlated with frictional strength (Scholz, 1968)and CFS (Gulia et al., 2018). Therefore, we also examine the correlation of Δp or *CFS* to *b*-value variation.

2.2 Natural Earthquakes and Laboratory Experiments Case

Here we briefly contrast the injection-induced seismicity setting described above with the geomechanical settings of natural earthquakes and laboratory experiments (see Figure 1b). In a natural earthquake case, we implicitly consider a fault that is well-oriented with a given stress condition, and for laboratory experiments case we also assumes a well-oriented-fault (a single preexisting fault or nucleated single fracture) (e.g., Goebel et al., 2012, 2013). In such situations, we don't need to consider the effect of intermediate principal stresses. On the smaller Mohr stress circle defined with S_1 and S_3 in Figure 1b, the stress state of the well-oriented fault is indicated by point 1. The small Mohr stress circle does not intersect the failure line. We consider the cases where the tectonic loading for a natural earthquake and the axial loading for laboratory seismicity change the stress state. In those cases, the failure line does not shift since the pore pressure is constant. We assume that the maximum principal stress (S_1) increases and that the minimum principal stress (S_3) is constant, resulting in a bigger Mohr stress circle. We also assume constant orientations for the principal stresses. The bigger Mohr stress circle intersects the failure line, where Point 2 in Figure 1b shows the new stress state of the same well-oriented fault. Shear and normal stresses on the well-oriented fault change from τ_1 and σ_{n1}, to τ_2 and σ_{n2}, respectively. This means that the frictional strength changes according to the change in differential stress. The brown arrow (from point 1 to point 2) shows the simplest *CFS* process (stress path). Note that we assume a simple example of loading conditions with a constant minimum principal stress. The process leading to an earthquake (stress path) is more complicated.

In summary, the process of overcoming a frictional strength differs between injection-induced seismicity and natural earthquakes. In the injection-induced seismicity case, the stress state (differential stress) is constant, but the pore pressure controls the initiation of failure. On the other hand, in the natural earthquake and laboratory experiment case, stress is the driving force. Thus, the physical meaning of *CFS* depends on the context. For injection-induced seismicity, *CFS* is just a different form of Δp. But for a natural earthquake, *CFS* correlates with differential stress (so, shear and normal stress). Therefore, *CFS* is a valuable parameter to correlate with the *b*-value in the natural earthquake setting (Gulia et al., 2018; Scholz, 1968). However, in the injection-induced seismicity setting differential stress is constant, we can expect no correlation between Δp (*CFS*) and *b*-value, because Δp (*CFS*) cannot influence differential stress.

3 Field Overview and Data

3.1 The Basel EGS Project

To investigate the *b*-value dependency on geomechanical parameters, we took the unique opportunity to study high-quality microseismic data and *in-situ* stress information from the Basel Enhanced Geothermal System (EGS) project. In 2006, hydraulic stimulation was performed for the injection well: Basel-1, to create an artificial geothermal reservoir. Geothermal Explores Ltd. (GEL) operated the entire project, including hydraulic stimulation and microseismic monitoring. Hydraulic stimulation lasted about six days beginning 2nd of December 2006, and 11,500 m^3 of water were injected into basement granite. The open-hole section of the injection well (4629–5000 m) was subject to stimulation, which resulted in fluid penetrating the surrounding granite formation through several permeable zones. A maximum wellhead pressure of 30 MPa was measured at a flow rate of 3300 L/min (Häring et al., 2008). Microseismic activity started when the wellhead pressure reached around 10 MPa. Then, roughly a 1 km^3 artificial reservoir had been created. On the 6th day of the stimulation, the largest induced seismic event, M_w 3.51, occurred despite a reduction in flow rate (Häring et al., 2008). This event was widely felt by the locals in Basel and invoked further risk analysis of the EGS project, which finally lead to a shutdown of the project.

Results from the Basel project have materially contributed to the understanding of induced seismicity. This EGS project was carried out in an urban area. Accordinglly, a sophisticated microseismic monitoring system was set up to observe the effects of the stimulation. Seismic velocity calibration, detailed borehole logging, and a dense surface network for monitoring were employed based on the experience of another European EGS experiment at Soultz (e.g., Baujard et al., 2014; Dorbath et al., 2009; Evans et al., 2005). The resulting data that were collected from the Basel project led to many studies on broad range of topics (Bachmann et al., 2011a; Catalli et al., 2013; Dyer et al., 2008; Folesky et al., 2016; Herrmann et al., 2019; Kraft et al., 2009; Mukuhira et al., 2013; Terakawa et al., 2012; Ziegler & Evans, 2020).

3.2 Microseismicity

The GEL microseismic monitoring network consisted of six downhole stations and one temporal station in the injection well. Three-component seismometers were installed in the six downhole stations. One of the downhole stations was placed in the granite section starting from 2265 m from the surface, which contributed to constraining the depth of hypocenters. One temporal station located in the injection well only operated for a few hours. Nevertheless, the recovered signal from that sensor was utilized for velocity model calibration (Dyer et al., 2008; Häring et al., 2008).

The GEL network captured around 13,000 events during and after stimulation, and hypocenters were determined for around 3,000 microseismic events with robust picks in near real-time (Dyer et al., 2008). Asanuma et al. (2007) also determined the absolute hypocenter locations of the microseismic events and got results consistent with those of Dyer et al. (2008). Then, Asanuma et al. (2008) applied a multiplet cluster analysis (Moriya et al., 2003), where relative hypocenter locations were determined using the double-difference method (Waldhauser & Ellsworth, 2000). The spatial error in the absolute hypocenter location was typically 40 m, and

the error in the relative location was less than 20 m. Like our previous studies (e.g., Mukuhira et al., 2021a), the current study is also based on the seismic catalog originally provided by GEL. That catalog contains the microseismicity that occurred from the start of the stimulation to June 2007.

The magnitudes of the microseismic events in our catalog are also based on the estimates by GEL. GEL estimated moment magnitudes (M_w) from the amplitude of P-waves in the time domain (Dyer et al., 2008), which were consistent with M_w estimates in the frequency domain (Dyer et al., 2010). A detailed explanation can be found in Mukuhira et al. (2017), and relation between M_w to local magnitude was discussed in Bethmann et al. (2011).

Some of the larger induced seismic events were additionally captured by the surface seismic network for monitoring natural earthquakes in Switzerland, operated by the Swiss Seismological Service (SED). Deichmann & Giardini (2009) reported the first results of fault plane solutions (FPSs) for several large events, and Terakawa et al. (2012) added more results of FPS estimation using SED data. Many FPSs showed a strike slip type focal mechanism, and some showed a normal fault type focal mechanism. In total, the FPSs of 118 large events are available for geomechanical analysis.

We further employed the results of multiplet cluster analysis to make more fault orientation information available. We applied multiplet cluster analysis to events grouped based on their waveform similarity by using the coherence function. We sorted the events based on similarities in their source functions (focal mechanism) and their Green functions (ray path and source region). Typically, the relocated hypocenters of multiplet cluster events indicate a very localized source region, and they delineated the shape of existing fractures. Many of the multiplet clusters exhibited planar and streak shapes. Then, we applied principal component analysis (PCA) to extract the normal vectors of the existing faults delineated by the multiplet clusters (Asanuma et al., 2007; Mukuhira et al., 2013; Mukuhira et a., 2021a). The robustness of the fault orientations obtained from cluster analysis is not as high as from the SED FPS, but they are consistent with the stress state and natural fracture distributions from borehole logging (Ziegler & Evans, 2020). Detail of the fault orientation information can be found in supplementary information.

Figure 2 shows the basic characteristics of microseismic activity at Basel. In all panels in Figure 2, the events that SED estimated FPSs for are shown with red circles. In the magnitude-time correlation (Figure 2a), we can observe that larger events specifically occurred on the 5^{th} and 6^{th} days. In Figure 2b, the depth migration of hypocenters is shown as a function of time. The microseismic activity started around the 4600 m depth and migrated both up and down. The larger events shown with red circles are located both shallower and deeper than the injection zone before the 6.5^{th} day. After shut-in on the 6^{th} day, the largest event occurred in the deeper part of the reservoir. The series of significant occurrences of large events was explained with the redistribution of pore pressure during the shut-in phase and seismic activity during the shut-in phase was peculiar to this field (Mukuhira et al., 2017). Figure 2c shows the hypocenter distribution along the North-South cross-sectional view of the reservoir. We do not see a significant local concentration in the hypocenters of the larger events. After the 11^{th} day from the start of stimulation, microseismic activity continued. The microseismic events occurred mainly in the shallower part of the reservoir, and the microseismic cloud still expanded upward.

For more details about fault orientations used in this study, please refer to our previous studies (Mukuhira et al., 2017, 2018, 2021a), where the same fault orientation information was utilized.

3.3 *In-situ* Stress Information

Basel is located at the southern end of the Rhine Graben and the fault system in the region consists of NNE, ENE, and NW striking faults (Häring et al., 2008). The regional earthquakes' focal mechanisms suggest a strike-slip stress state with a NW-SE orientation of the maximum horizontal stress (S_{Hmax}). Borehole breakout analysis was performed on the logging images from the granite section of the deepest monitoring well (OT-2) and the injection well (Basel-1). The results suggest that the estimates of the orientation of S_{Hmax} from two boreholes are consistent with an estimated orientation of N144E±14° (Häring et al., 2008; Valley & Evans, 2009).

Our previous studies (e.g., Mukuhira et al., 2021a) used the *in-situ* stress model proposed by Valley & Evans, (2015). In this study, we use the updated *in-situ* stress model by Valley & Evans (2019). We evaluated the effect of updated *in-situ* stress model on geomechanical parameters (Supplementary information). Stress magnitudes were inferred from borehole breakout analysis (Valley & Evans, 2019). The analysis resulted in an *in-situ* stress model as a function of depth *z* in m where

$$\boldsymbol{S_{Hmax} = 0.005z + 90} \quad (8)$$

$$\boldsymbol{S_{hmin} = 0.007z + 42} \quad (9)$$

$$\boldsymbol{S_{v} = 0.0249z} \quad (10),$$

Here S_{hmin} is minimum horizontal stress. The unit for stress is MPa. The vertical stress S_{v} was estimated as lithostatic based on a density log (Valley & Evans, 2015). S_{hmin} and S_{Hmax} were determined from borehole break out analysis considered with drilling induced tension fractures and several failure criteria (Valley & Evans, 2019). This stress model is shown as a function of depth in Figure 3a. As S_{Hmax} has a small gradient, a stress transition occurs at around 4550 m. So, in the shallower part of the reservoir, the stress state is a strike-slip type, but in deeper parts of the reservoir, the stress state is a normal-fault type. We calculate the differential stress at each depth, as shown in Figure 3a. The differential stress decreases slightly with depth until the stress state transition point, and then increases slightly again having larger value at deeper depth. The variation in differential stress (39~49 MPa) is also caused by the small gradient of S_{Hmax}.

We investigate the *b*-value dependency on the aforementioned geomechanical parameters based on this stress model. We assume that this stress model is valid in the study area of the reservoir, meaning that the stress state is laterally uniform, since our previous study showed several types of evidence supporting laterally homogeneous stress state in the study area (Mukuhira et al., 2017). We compute Δp and *CFS* under the assumption that all seismicity was triggered by the increase in pore pressure. Here, we don't consider other possible triggering

mechanisms such as thermal stresses, static stress changes, and poroelastic stress effects. Our study area is a 1 km^3 fractured reservoir, which was stimulated for one week by hydraulic stimulation, so that considering the pore pressure increase by fluid flow as the main triggering mechanism is a reasonable assumption (Mukuhira et al., 2017). We investigated the uncertainty in the stress model based on statistics and its influence on Δp, we found that the possible uncertainty in Δp with a friction coefficient of 0.6 was not negligilble, but comparison with other physical constraints of the wellhead pressure proved that Δp values were reasonably estimated and the uncertainty in Δp was not so significant (Mukuhira et al., 2017).

4 Results

4.1 Correlation Between Magnitude and Geomechanical Parameters

First, we investigated the correlation between geomechanical parameters and the event magnitude. Figure 3b shows the depth distribution of event magnitudes, and we cannot observe any significant magnitude trend with depth. We observed some events with M_w>2.5 in deeper (>4900 m) and shallower (<4300 m) parts of the reservoir, but many of them occurred during the shut-in phase (Figure 2b). Figure 3c shows the depth profile of resolved shear stress on fault. There are two types of plots showing the shear stress estimated from FPS (orange) and cluster analysis (blue). The linear streaks of blue markers are due to our assumption that all members of a cluster have the same fault orientation, so events in the same cluster have similar shear stresses. Furthermore, most of the clusters display vertical planar or streak shapes that lead to this plot result.

To remove the effect of depth dependent differential stress, we introduce the measure of normalized shear stress: NSS (Mukuhira et al., 2020a). Then, we can investigate the geomechanical characteristics of the existing faults without influence of the slightly varying differential stress. The NSS is the ratio between the shear stress and the maximum shear stress at a depth of the event. So, in practice, we divide the shear stress value by half of the differential stress (radius of Mohr stress circle). NSS indicates the relative height of the point showing the stress state of the fault on the Mohr stress circle. Note that 0.87, 0.76, and 0.71 are the NSSs corresponding to the well-oriented faults for friction coefficients of 0.6, 0.85, and 1.0. Thus, by using NSS (see Figure 3d) we remove the trend in the maximum shear stress in Figure 3c. The observed maximum NSS starts deviating from 1 for depths>4550, suggesting that from the reservoir deeper than 4550 m, the faults oriented to have higher NSS were not triggered for some reason such as that sufficient pore pressure had not been reached or simply there were no such existing faults.

Then, we compute Δp with equation (2) and *CFS* with equation (5). We used a friction coefficient of 0.6 as in our previous studies (Mukuhira et al., 2017a, b). As with the case of the depth dependency of shear stress, we observe a systematic decrease in the lower bound for Δp, especially for depth>4550 m (Figure 4b), and a systematic increase in the upper bound for *CFS* as a function of increasing depth (Figure 4c). Since the minimum Δp (green lines) at a depth corresponds to the Δp of a well-oriented fault, these trends are showing the effect of the differential stress. Differential stress corresponds to the diameter of the Mohr stress circle. If the

Mohr stress circle becomes bigger, a well-oriented fault will have a shear slip for a smaller Δp in general. We find that Δp values for some large events are away from the minimum Δp. However, in the deeper part of the reservoir, most of the larger events occurred close to the minimum Δp. Again, we observe slight deviation of the observed Δp from the minimum Δp expected based on the stress model (green line).

We first directly compare event magnitudes with geomechanical parameters. Figure 5 shows the relationship between magnitude and the shear and normal stresses, and their normalized forms. We also normalize the normal stress using the differential stress at the depth of the event as $(\sigma_n\text{-}S_3)/(S_1\text{-}S_3)$. The normal stress ranges from the minimum principal stress (S_3) to the maximum principal stress (S_1), so we normalized the absolute normal stress by the differential stress ($S_1\text{-}S_3$).

There is a clear correlation between NSS and magnitude in Figure 5a; e.g., big events occurred along faults with high NSS. We found the same result in our previous work which used an previous version of the *in-situ* stress model (Mukuhira et al., 2020). That observation was the motivation to investigate the *b*-value dependency on shear stress. Note that the critical relationship between geomechanical parameters and magnitude are not essentially influenced by the difference of *in-situ* stress models (please refer to the supplementary information). The correlation between absolute shear stress and magnitude in Figure 5b is clearer than that between NSS and magnitude.

The relationship between magnitude and normal stress is shown in Figures 5c and 5d. We cannot confirm any significant correlation between magnitude and normal stress or its normalized form. When shear slip occurs on a fault, the normal stress (effective normal stress) has decreased to the frictional strength level. Even though the initial normal stress was high, it is not relevant at the initiation of shear slip. Also, the normal stress works perpendicular to the slip direction. Therefore, no correlation between magnitude and normal stress would be expected from a static geomechanical point of view.

We further investigate the correlation between the magnitude and other geomechanical parameters. Figure 6a shows the relationship between magnitude and differential stress. The relationship shown here is similar to the depth magnitude relationship since the differential stress is a function of depth though it is not a simple monotonically decreasing linear function with depth. There is no clear correlation or tendency, with some large events occurring at a depth of small differential stress, and we can see several larger events that occurred at depths where differential stress > 46 MPa. The observations presented in Figure 6a are similar to Figure 3 since differential stress correlates with depth.

In Figures 6b and 6c, we compare the magnitude with Δp and *CFS*. As we explained in the previous section, Δp and *CFS* are essentially interchangeable, so we focus on Δp. The magnitude distributes almost homogeneously with Δp. We may plausibly find a weak correlation between Δp and magnitude from our visual observation, which is not entirely same with our expectation from theory discussed in section 2.1. But the correlation is not as clear as the correlation between shear stress or NSS and magnitude. This observed correlation is not surprising since the definition of Δp includes shear stress as showed in equation (2), but the correlation to the shear stress has been masked due to the effect of normal stress. We consider

that still some part of the data resulted in this weak correlation (please see the supplementary information for the liner relationship between shear or normal stress and Δp).

4.2 The *b*-value Dependency on Geomechanical Parameters

4.2.1 Method

In the previous section, we observed some correlation between magnitude and geomechanical parameters from a simple comparison of the parameters and a visual check. To further investigate those correlations and find the key parameter responsible for the *b*-value dependency in the injection-induced seismicity setting, we checked the correlation between *b*-value and geomechanical parameters.

In the following analysis, we estimate *b*-values with the maximum likelihood method (Aki, 1965; Utsu, 1999), and the binning size for magnitudes is 0.1. The uncertainty (standard deviation) in the *b*-value is estimated with the method proposed by Shi & Bolt (1982). Magnitude completeness (Mc) is also an important parameter for estimating the *b*-value. We use a constant Mc for all *b*-value estimates. Of course, we could estimate Mc for each sub-catalog, but Mc sometimes varies significantly between sub-catalogs, according to the events included in it. Instead of estimating an optimal Mc for each sub-catalog, we choose several constant Mc values (Mc=0.7, 0.8, 0.9, and 1.0). We will estimate the *b*-value for bins defined by a moving window along each geomechanical parameter. Bins contain some events tht fall in multiple bins according to the window size and shift, which suggests that our binning contains a moving average effect. The bin size is constant and chosen to provide large enough event sample sizes. We estimate the *b*-value only when the bin contains more than 100 events larger than Mc. We show the number of the events used for *b*-value estimation along with *b*-value estimates in the following analysis and we used much more than 100 events for *b*-value estimation in most of the cases.

4.2.2 Depth

The *b*-value dependency on depth is examined in Figure 7. We estimate the *b*-values for different depths at 100 m intervals with 200 m wide bins. From Figure 7b, the *b*-value shows a higher value near the injection depth of 4600 m. The *b*-value at the shallow and deep parts of reservoir have lower estimated values. In the depth of higher *b*-values, the number of events used for *b*-value estimation is also larger. A large number of events occurred at a depth range close to the depth of the injection point throughout the stimulation period resulting in the large number of the events.

4.2.3 Normalized Shear Stress and Absolute Shear stress

Compared to our previous study (Mukuhira et al., 2021a), we investigate the *b*-value dependency in a different way. We estimate the *b*-values every 0.05 NSS with a 0.2 bin width. Figure 8a shows the correlation between the *b*-value and NSS, showing a clear dependency, except for the case of Mc=1.0. The *b*-value increased after the bin center reached 0.9, but overall dependency is evident as the correlation coefficients show. The number of events increases after the bin center reaches 0.8 but still there are not so many events available for *b*-value estimation in the case of Mc=1.0. This allowed *b*-value estimation only for NSS>0.75 for the case of

Mc=1.0. There is a gap around NSS=0.4. This is due to the lack of data around NSS=0.4, as shown in Figure 5a. These results, which were found using an updated *in-situ* stress model, strongly support the conclusion from Mukuhira et al. (2020) that the *b*-value decreases with increasing normalized shear stress.

Figure 8c shows the *b*-value dependency on absolute shear stress, where we estimate *b* for every 1 MPa with 5 MPa wide bins. We can confirm a clear dependency here again except for the case of Mc=1.0, for which there are not enough events to draw conclusions from. The dependency is clearer than that for NSS as the correlation coefficients show. We considered that NSS is better than absolute shear stress for characterizing *b*-value dependency since we can ignore the minor fluctuation in differential stress, but absolute shear stress shows a clearer correlation with magnitude from Figure 5a and 5b. Here absolute shear stress seems to show a clearer correlation with *b*-value than NSS does.

4.2.4 Differential Stress

Figure 9a shows the estimated relationship between the *b*-value and differential stress, where we estimate the *b*-value every 1 MPa with 4 MPa wide bins. The *b*-value shows a higher value for differential stresses around 42–43 MPa. Then the *b*-value becomes lower for smaller and larger differential stresses. This bahavior is originated in the correlation between the *b*-value and depth as we discussed in 4.2.2. The differential stress is varied with depth (Figure 3a), and the correlation of *b*-value to differential stress reflects the correlation of *b*-value to depth. From these results, differential stress does not appear to be a good parameter to explain *b*-value variability, which is consistent with our expectation and the fact that the observed range of differential stress values is narrow.

4.2.5 Pore Pressure Increase & *CFS*

Figures 9c and 9e show the *b*-value dependency on the relative stress index to the failure in the form of Δp and *CFS*. Those figures 9c and 9e show the same tendency, although they are bilaterally symmetrical. Both of them show weak correlations. In the case of Δp, we can observe that the *b*-value does not change significantly at 9~19 MPa where a sufficient number of events are available for *b*-value estimation. For higher Δp, the *b*-value increase can be observed only for the lowest Mc case, where *b*-value estimation is less stable due to smaller number of events triggered by higher Δp. We can observe the same behavior for *CFS*, and correlation is clearer in the case of *CFS* probably because we used a wide window. Correlation coefficients between *CFS* and the *b*-value show quite high values, but those between shear stress and *b*-value are much higher. From this analysis, unlike our expectation, Δp and *CFS* appear to correlate with the *b*-value. However, observed correlation is not as clear as that between NSS or shear stress and *b*-value. It is difficult to interpret the weak correlation between Δp and the *b*-value since there is no clearer correlation between Δp and magnitude as shown in Figure 6c.

5 Discussion

5.1 Shear Stress is Responsible for *b*-value Variation

We found that NSS and shear stress clearly showed systematic correlation with the magnitude of induced seismicity, and that the *b*-value also clearly correlated with NSS and shear stress. The *b*-value dependency on NSS or shear stress was much clearer than the relationship between the *b*-value and any other geomechanical parameters, including differential stress and Δp. These observations strongly support and comprehensively follow up on the conclusion from Mukuhira et al. (2021a) that the *b*-value is negatively correlated to NSS or shear stress.

The *b*-value is commonly considered to negatively correlate with differential stress in natural earthquake and laboratory studies (Amitrano, 2003; Goebel et al., 2013; Scholz, 1968; Scholz, 2015; Wiemer & Wyss, 1997). In our case, due to the difference in the tectonic loading setting, the differential stress does not actively change during fluid injection. In fact, the inherent differential stress variability in our stress model is around 10 MPa (differential stress range of 39-49 MPa), and the absolute value of differential stress in our model is considerably smaller than the differential stress expected in a natural earthquake region (Scholz, 2015) and in lab experiments (Amitrano, 2003; Goebel et al., 2013; Scholz, 1968). We did not observe a clear dependency of the *b*-value on the differential stress, nor did we notice a simple correlation between magnitude and differential stress. So, the differential stress is not the main cause of the *b*-value reduction for injection-induced seismicity as we expected based on geomechanical theory. This could be simply because the differential stress is nearly constant even though pore pressure increases due to hydraulic injection.

The *b*-value dependency was initially discussed in relation to the relative stress index to the failure (frictional strength) (Scholz, 1968). Following studies discussed *b*-value dependency on differential stress. We already argued in section 2 that pore pressure which is the relative stress index to the failure in the injection-induced seismicity setting does not function in the same manner as differential stress or frictional strength in a natural earthquake case because pore pressure cannot change the differential stress. *CFS* in injection induced seismicity setting purely behaves as Δp. Pore pressure increase just prompts the failure. So, the pore pressure cannot affect the *b*-value. This is also valid even in a natural earthquake settings since pore pressure still cannot change differential stress. In contrast to our expectation, however, the *b*-value shows some correlation to Δp, but the correlation between Δp and the *b*-value was not as clear as that between shear stress and the *b*-value. Required pore pressure for failure is related to shear stress by equation (2). Therefore, correlation between shear stress and the *b*-value can still be observed in the form of Δp but the correlation is weakened by the effect of normal stress.

From the geomechanical theory and the observations, we conclude that, in an EGS or injection-induced seismicity setting, *b*-value variation is significantly correlated to shear stress or NSS rather than differential stress or Δp (or *CFS*). This is because the shear stress behaves as differential stress, which correlates with *b*-value reduction in natural earthquake or laboratory settings. In addition, Δp affect neither shear stress nor differential stress. So, we conclude that the events from the faults oriented to have higher shear stress are the cause of the *b*-value reduction. We would like to note that we found that NSS and the shear stress are essentially the same in the in-situ stress setting of this study, although we introduced NSS to completely remove the influence of depth dependent differential stress and stress state transition.

5.2 Dynamic Behavior of the *b*-value

We have investigated *b*-value dependency using a static catalog and geomechanical data without considering event times or location, apart from depth. We tested whether our first conclusion that *b*-value reduction is caused by the events along high NSS faults is consistent with the *b*-value variation in time and space. We can hypothesize that the *b*-value reduction happens when more events occur along high NSS faults. The stress states of the faults that have high NSS are plotted to the right of and higher on the Mohr stress circle than the point of a well-oriented fault (Figure 1a). So, high NSS faults require a larger Δp than the minimum Δp for a well-oriented fault, suggesting that the *b*-value should decrease with the relevant pore pressure increase.

Figure 10 shows time series of the hydraulic injection parameters, magnitude, NSS, the fraction of the number of events within different NSS ranges, and *b*-values. From Figure 10f we can visually observe that many events occurred along high NSS faults. We don't observe a drastic increase with time in the number of events along higher NSS faults (Figure 10f). But the fraction of events from lower NSS faults decreases with time, and it falls below 0.5 at 4.5 days, suggesting that the majority of the event occurred from higher NSS faults (NSS>0.71).

We estimate the *b*-value every 0.5 days with a time window length of 1 day, as shown in Figure 10c. The *b*-value appears to be nearly constant from the first until the 4th day of the stimulation, and then, the *b*-value starts decreasing after 4.5 days when the wellhead pressure reached 20 MPa. The *b*-value is still decreasing after the shut-in phase, and it starts increasing after 8 days. In Figure 10d, we also estimate the *b*-value for each event occurrence time using the previous 100 events. We observe dynamic variations in the estimated *b*-values. All of the *b*-value results for each Mc show a decreasing trend toward the shut-in phase, which starts around 6.5 days. The *b*-values estimated with smaller Mcs show a very dynamic behavior, but the *b*-values estimated with larger Mc =1.0 shows more stable behavior. This is because the inclusion of larger events in a time window may affect the average of magnitude in maximum likelihood estimation of the *b*-value (Aki, 1965).

Focusing on the period before the shut-in, we can observe that the *b*-value decreases with the increase in wellhead pressure. This pressure increase can cause shear slip on the faults having higher NSS values. The *b*-value reduction with increasing wellhead pressure and the increasing number of events from higher NSS faults (Figure 10f) are synchronously correlated with respect to time. So, our working hypothesis is verified by those observations. Note that the *b*-value correlation to wellhead pressure should depend on the population distribution of existing fractures since a larger Δp can cause not only higher NSS faults but also lower NSS faults to slip as indicated with point 2 and 3 in Figure 1a. In this case, we could observe the correlation between wellhead pressure and *b*-value, since there would be many existing faults having higher NSS that would slip (Häring et al., 2008; Ziegler & Evans, 2020).

Another interesting observation is that the *b*-values significantly decrease before the occurrence of the largest event in the shut-in phase on day7 (see Figure 2), even though the wellhead pressure started decreasing due to the pressure bleed-off (Figure 10a, b). We investigated the pore pressure migration behavior at the shut-in phase and found that pore pressure still migrated farther at the edge of the seismic cloud (Mukuhira et al., 2017). The significant *b*-value decrease before the largest event also would be correlated with the higher NSS faults, which were activated by shut-in pore pressure migration. The significant drop of *b*-

596 value around 6.5 days does not follow the same trend as before (Figure 10d). We also consider
597 that shut-in pore pressure migration enhances the *b*-value reduction. From our interpretation,
598 pore pressure redistribution during the the shut-in phase also cannot change the differential
599 stress, and it only enhances the occurrence of seismicity especially from the faults with higher
600 shear stress.

601 Bachmann et al. (2011, 2012) conducted an innovative seismo-statistical analysis of the
602 Basel microseismic data. They found a systematic decrease of *b*-value with time and distance
603 from the injection point, as the first case study of injection-induced seismicity. Bachmann et al.
604 (2012) employed a simple geomechanical model that included pore pressure migration that led to
605 a prediction of a variation of differential stress from 20 to 150 MPa by stress heterogeneity along
606 well-oriented existing faults. They concluded that the *b*-value variation was caused by variability
607 in differential stress. We have a different interpretation and we have reasons to support our stress
608 model (e.g., Mukuhira et al., 2017) rather than strong heterogeneity in *in-situ* stress. Considering
609 the fact that pore pressure cannot change the differential stress, the observed *b*-value variation
610 needs another explanation other than differential stress or pore pressure (wellhead pressure).
611 That is shear stress. We have shown that the shear stress correlates with *b*-value variation better
612 than any other geomechanical parameters. So, this study successfully extends the understanding
613 of the mechanism behind the correlation between pore pressure and the *b*-value, and provides a
614 profound understanding of the cause of the *b*-value variation for injection-induced seismicity.

615

616 **5.3 *b*-value Behavior in Earthquake Swarms**

617 Recently natural earthquake swarm studies discovered that fluid migration from a deeper
618 part of the crust played a very important role in swarm activity (e.g., Okada et al., 2015; Shelly et
619 al., 2016; Yoshida et al., 2016, 2017). The phenomena of natural earthquake swarms and
620 injection-induced seismicity have a lot of similarities, such as migration of hypocenters and
621 interaction with pore pressure. Yoshida et al. (2017) analyzed an earthquake swarm near the
622 Yamagata-Fukushima border after the 2011 Tohoku-Oki earthquake and found a correlation
623 between temporal changes in the *b*-value and frictional strength variation. Note that frictional
624 strength in their study is equivalent to our NSS since they assumed uniform stress conditions in
625 the study area, so the *b*-value correlation to frictional strength is caused by the variation of the
626 focal mechanism (Yoshida et al., 2017). This is exactly the same conclusion that we made for
627 our injection-induced seismicity observations. Therefore, despite the different data and different
628 approaches, both this study and Yoshida et al.（2017) found that *b*-value reduction can be caused
629 by events from high shear stress faults (frictional strength) instead of variations in differential
630 stress. Our concluisons apply to cases where we can assume a uniform stress state and a non-
631 tectonic triggering driving force such as fluid injection or pore pressure migration from
632 dehydration.

633

634 **6 Conclusions**

We have investigated the correlation between the *b*-value and geomechanical parameters using injection-induced microseismic data from the Basel, Switzerland, EGS project and in-situ stress data acquired from borehole logging analysis. From the fault orientation and *in-situ* stress information, we estimated the shear stress, normal stress, pore pressure increase, and Coulomb failure stress for each existing fault that caused observed microseismicity. We considered that the *in-situ* stress model was valid in the study area of a 1 km^3 reservoir and that all of the induced seismicity was triggered only by pore pressure increase. So, we investigated the alternative explanation for the *b*-value variation in injection-induced seismicity beyond the well-accepted correlation between the *b*-value and differential stress, since the differential stress is nearly constant for the Basel case.

From the simple comparison between magnitude of microseismic events and the geomechanical parameters that we evaluated, we found that event magnitude systematically correlated with the normalized form of shear stress and also shear stress. Other geomechanical parameters did not show meaningful correlation with event magnitude. Then, we further investigated this correlation with a *b*-value analysis. The *b*-value analysis demonstrated that the *b*-value systematically correlated with the shear stress, but the *b*-value did not show a clear correlation with other geomechanical parameters. Thus, we concluded that the *b*-value reduction for injection-induced seismicity is caused by events from high shear-stress faults. We also observed that the *b*-value decreased with an increasing number of events that had high shear stress, which strongly supports our conclusion.

We have discovered that new relationship between shear stress and *b*-value variation in the injection-induced seismicity case where significant variation in differential stress is not expected. Due to the difficulty of stress measurement at the depths of most natural earthquakes, the physics behind *b*-value variation had not been studied with reliable *in-situ* stress information. This study fully utilized a unique opportunity to investigate the *b*-value dependency on geomechanical parameters comprehensively by combining the seismological data and directly measured *in-situ* stress data. The insights from this study fill the gap in the *b*-value physical mechanism understanding from the laboratory scale to the field scale. This work may also contribute to the safe operation of fluid injection in EGS, CCS (carbon capture and storage), and unconventional reservoir development by avoiding unnecessary high wellhead pressure injection that can reactivate faults of high shear stress. Using the NSS index would be the better way to evaluate the *b*-value change by the occurrence of events from different faults without effects from stress field change. We also would like to highlight the importance of *in-situ* stress measurements, which provide invaluable information for seismic hazard assessment in reservoir engineering and the scientific understanding of induced seismicity.

Acknowledgments

We thank Geo Explorers Ltd. and Geo-Energie Suisse AG for providing the microseismic wave data sets. We are also grateful to the editor and reviewers for their constructive comments. We thank K. Yoshida, K. Okamoto, X. Ma, and H. Moriya for discussions and comments on the manuscript. All authors are not aware of any conflict of interest. This study was supported by Grant-in-Aid for Scientific Research(C): 20K05394.

Data Availability Statement

The microseismic catalog data containing the location, magnitude and cluster information are available in Mukuhira et al. (2021b). *In-situ* stress data and focal mechanisms are available from previous literature (Deichmann & Giardini, 2009; Terakawa et al., 2012; Valley & Evans, 2009, 2015, 2019).

References

Aki, K. (1965). Maximum Likelihood Estimate of b in the Formula logN=a-bM and its Confidence Limits. *Bull. Earthq. Res. Inst.*

Amitrano, D. (2003). Brittle-ductile transition and associated seismicity: Experimental and numerical studies and relationship with the b value. *Journal of Geophysical Research*, *108*, 1–15. https://doi.org/10.1029/2001JB000680

Bachmann, C. E., Wiemer, S., Woessner, J., & Hainzl, S. (2011a). Statistical analysis of the induced Basel 2006 earthquake sequence: Introducing a probability-based monitoring approach for Enhanced Geothermal Systems. *Geophysical Journal International*, *186*(2), 793–807. https://doi.org/10.1111/j.1365-246X.2011.05068.x

Bachmann, C. E., Wiemer, S., Woessner, J., & Hainzl, S. (2011b). Statistical analysis of the induced Basel 2006 earthquake sequence: Introducing a probability-based monitoring approach for Enhanced Geothermal Systems. *Geophysical Journal International*, *186*(2), 793–807. https://doi.org/10.1111/j.1365-246X.2011.05068.x

Bachmann, C. E., Wiemer, S., Goertz-Allmann, B. P., & Woessner, J. (2012). Influence of pore-pressure on the event-size distribution of induced earthquakes. *Geophysical Research Letters*, *39*(9), 1–7. https://doi.org/10.1029/2012GL051480

Baujard, C., Schoenball, M., Kohl, T., & Dorbath, L. (2014). Large magnitude events during injections in geothermal reservoirs and hydraulic energy: A heuristic approach. *Geothermics*, *52*, 140–152. https://doi.org/10.1016/j.geothermics.2014.07.002

Beeler, N. M., Simpson, R. W., Hickman, S. H., & Lockner, D. A. (2000). Pore fluid pressure, apparent friction, and Coulomb failure. *Journal of Geophysical Research: Solid Earth*, *105*(B11), 25533–25542. https://doi.org/10.1029/2000jb900119

Bethmann, F., Deichmann, N., & Mai, P. M. (2011). Scaling relations of local magnitude versus moment magnitude for sequences of similar earthquakes in Switzerland. *Bulletin of the Seismological Society of America*, *101*(2), 515–534. https://doi.org/10.1785/0120100179

Catalli, F., Meier, M. A., & Wiemer, S. (2013). The role of Coulomb stress changes for injection-induced seismicity: The Basel enhanced geothermal system. *Geophysical Research Letters*, *40*(1), 72–77. https://doi.org/10.1029/2012GL054147

Deichmann, N., & Giardini, D. (2009). Earthquakes Induced by the Stimulation of an Enhanced Geothermal System below Basel (Switzerland). *Seismological Research Letters*, *80*(5), 784–798. https://doi.org/10.1785/gssrl.80.5.784

Dorbath, L., Cuenot, N., Genter, A., & Frogneux, M. (2009). Seismic response of the fractured

and faulted granite of Soultz-sous-For??ts (France) to 5 km deep massive water injections. *Geophysical Journal International*, *177*(2), 653–675. https://doi.org/10.1111/j.1365-246X.2009.04030.x

Dyer, B. C., Schanz, U., Ladner, F., Häring, M. O., & Spillman, T. (2008). Microseismic imaging of a geothermal reservoir stimulation. *The Leading Edge*, *27*(7), 856. https://doi.org/10.1190/1.2954024

Dyer, B. C., Schanz, U., Spillmann, T., Ladner, F., & Häring, M. O. (2010). Application of microseismic multiplet analysis to the Basel geothermal reservoir stimulation events. *Geophysical Prospecting*, *58*(5), 791–807. https://doi.org/10.1111/j.1365-2478.2010.00902.x

van der Elst, N. J., Page, M. T., Weiser, D. A., Goebel, T. H. W., & Hosseini, S. M. (2016). Induced earthquake magnitudes are as large as (statistically) expected. *Journal of Geophysical Research: Solid Earth*, *121*(6), 4575–4590. https://doi.org/10.1002/2016JB012818

Evans, K. F., Moriya, H., Niitsuma, H., Jones, R. H., Phillips, W. S., Genter, A., et al. (2005). Microseismicity and permeability enhancement of hydrogeologic structures during massive fluid injections into granite at 3 km depth at the Soultz HDR site. *Geophysical Journal International*, *160*(1), 388–412. https://doi.org/10.1111/j.1365-246X.2004.02474.x

Folesky, J., Kummerow, J., Shapiro, S. A., Häring, M., & Asanuma, H. (2016). Rupture directivity of fluid induced microseismic events: Observations from an enhanced geothermal system. *Journal of Geophysical Research: Solid Earth*, 1–14. https://doi.org/10.1002/2016JB013078

Goebel, T. H. W., Becker, T. W., Schorlemmer, D., Stanchits, S., Sammis, C., Rybacki, E., & Dresen, G. (2012). Identifying fault heterogeneity through mapping spatial anomalies in acoustic emission statistics. *Journal of Geophysical Research: Solid Earth*, *117*(3), 1–18. https://doi.org/10.1029/2011JB008763

Goebel, T. H. W., Schorlemmer, D., Becker, T. W., Dresen, G., & Sammis, C. G. (2013). Acoustic emissions document stress changes over many seismic cycles in stick-slip experiments. *Geophysical Research Letters*, *40*(10), 2049–2054. https://doi.org/10.1002/grl.50507

Goertz-Allmann, B. P., Goertz, A., & Wiemer, S. (2011). Stress drop variations of induced earthquakes at the Basel geothermal site. *Geophysical Research Letters*, *38*(9), 1–5. https://doi.org/10.1029/2011GL047498

Gulia, L., Rinaldi, A. P., Tormann, T., Vannucci, G., Enescu, B., & Wiemer, S. (2018). The Effect of a Mainshock on the Size Distribution of the Aftershocks. *Geophysical Research Letters*, *45*(24), 13,277-13,287. https://doi.org/10.1029/2018GL080619

Gutenberg, B., & Richter, C. F. (1944). Frequency of earthquakes in California. *Bulletin of the Seismological Society of America*, *34*, 185–188.

Häring, M. O., Schanz, U., Ladner, F., & Dyer, B. C. (2008). Characterisation of the Basel 1 enhanced geothermal system. *Geothermics*, *37*(5), 469–495. https://doi.org/10.1016/j.geothermics.2008.06.002

Herrmann, M., Kraft, T., Tormann, T., Scarabello, L., & Wiemer, S. (2019). A Consistent High-Resolution Catalog of Induced Seismicity in Basel Based on Matched Filter Detection and Tailored Post-Processing. *Journal of Geophysical Research: Solid Earth*, *124*(8), 8449–8477. https://doi.org/10.1029/2019JB017468

Ide, S., Yabe, S., & Tanaka, Y. (2016). Earthquake potential revealed by tidal influence on earthquake size–frequency statistics. *Nature Geoscience*, *9*(September), 10–14. https://doi.org/10.1038/ngeo2796

Kagan, Y. Y. (1999). Universality of the Seismic Moment-frequency Relation. *Seismicity Patterns, Their Statistical Significance and Physical Meaning*, *155*, 537–573. https://doi.org/10.1007/978-3-0348-8677-2_16

Kanamori, H., & Brodsky, E. E. (2004). The physics of earthquakes. *Reports on Progress in Physics*, *67*(8), 1429–1496. https://doi.org/10.1088/0034-4885/67/8/R03

Kraft, T., Mai, P. M., Wiemer, S., Deichmann, N., Ripperger, J., Kästu, P., et al. (2009). Enhanced geothermal systems: Mitigating risk in urban areas. *Eos*, *90*(32), 273–274. https://doi.org/10.1029/2009EO320001

McGarr, A. (2014). Maximum magnitude earthquakes induced by fluid injection. *Journal of Geophysical Research: Solid Earth*, *119*, 1008–1019. https://doi.org/10.1002/2013JB010597.Received

Mori, J., & Abercrombie, R. E. (1997). Depth dependence of earthquake frequency-magnitude distributions in California: Implications for rupture initiation. *Journal of Geophysical Research-Solid Earth*, *102*(B7), 15081–15090. https://doi.org/Doi 10.1029/97jb01356

Moriya, H., Niitsuma, H., & Baria, R. (2003). Multiplet-Clustering Analysis Reveals Structural Details within the Seismic. *Bulletin of the Seismological Society of America*, *93*(4), 1606–1620. https://doi.org/10.1785/0120020072

Mukuhira, Y., Dinske, C., Asanuma, H., Ito, T., & Häring, M. O. (2017). Pore pressure behavior at the shut-in phase and causality of large induced seismicity at Basel, Switzerland. *Journal of Geophysical Research: Solid Earth*, *122*(1), 411–435. https://doi.org/10.1002/2016JB013338

Mukuhira, Y., Fuse, K., Naoi, M., Fehler, M. C., Moriya, H., Ito, T., et al. (2018). Hybrid focal mechanism determination: Constraining focal mechanisms of injection induced seismicity using in situ stress data. *Geophysical Journal International*, *215*(2), 1427–1441. https://doi.org/10.1093/GJI/GGY333

Mukuhira, Y., Fehler, M. C., Ito, T., Asanuma, H., & Häring, M. O. (2021). Injection-Induced Seismicity Size Distribution Dependent on Shear Stress. *Geophysical Research Letters*. https://doi.org/10.1029/2020GL090934

Mukuhira, Yusuke, Asanuma, H., Niitsuma, H., & Häring, M. O. (2013). Characteristics of large-magnitude microseismic events recorded during and after stimulation of a geothermal reservoir at Basel, Switzerland. *Geothermics*, *45*, 1–17. https://doi.org/10.1016/j.geothermics.2012.07.005

Mukuhira, Yusuke, Moriya, H., Ito, T., Asanuma, H., & Häring, M. (2017). Pore pressure migration during hydraulic stimulation due to permeability enhancement by low-pressure

799 subcritical fracture slip. *Geophysical Research Letters*, *44*(7), 3109–3118.
800 https://doi.org/10.1002/2017GL072809

801 Nanjo, K. Z., & Yoshida, A. (2018). A b map implying the first eastern rupture of the Nankai
802 Trough earthquakes. *Nature Communications*, *9*(1), 3–6. https://doi.org/10.1038/s41467-
803 018-03514-3

804 Nanjo, K. Z., Hirata, N., Obara, K., & Kasahara, K. (2012). Decade-scale decrease in b value
805 prior to the M9-class 2011 Tohoku and 2004 Sumatra quakes. *Geophysical Research*
806 *Letters*, *39*(20), 3–6. https://doi.org/10.1029/2012GL052997

807 Nishikawa, T., & Ide, S. (2014). Earthquake size distribution in subduction zones linked to slab
808 buoyancy. *Nature Geoscience*, *7*(December), 904–908. https://doi.org/10.1038/ngeo2279

809 Okada, T., Matsuzawa, T., Umino, N., Yoshida, K., Hasegawa, A., Takahashi, H., et al. (2015).
810 Hypocenter migration and crustal seismic velocity distribution observed for the inland
811 earthquake swarms induced by the 2011 Tohoku-Oki earthquake in NE Japan: Implications
812 for crustal fluid distribution and crustal permeability. *Geofluids*, *15*(1–2), 293–309.
813 https://doi.org/10.1111/gfl.12112

814 Petruccelli, A., Gasperini, P., Tormann, T., Schorlemmer, D., Rinaldi, A. P., Vannucci, G., &
815 Wiemer, S. (2019). Simultaneous Dependence of the Earthquake-Size Distribution on
816 Faulting Style and Depth. *Geophysical Research Letters*, *46*(20), 11044–11053.
817 https://doi.org/10.1029/2019GL083997

818 Petruccelli, A., Schorlemmer, D., Tormann, T., Rinaldi, A. P., Wiemer, S., Gasperini, P., &
819 Vannucci, G. (2019). The influence of faulting style on the size-distribution of global
820 earthquakes. *Earth and Planetary Science Letters*, *527*, 115791.
821 https://doi.org/10.1016/j.epsl.2019.115791

822 Pine, R. J., & Batchelor, A. S. (1984). Downward migration of shearing in jointed rock during
823 hydraulic injections. *International Journal of Rock Mechanics and Mining Sciences And*,
824 *21*(5), 249–263. https://doi.org/10.1016/0148-9062(84)92681-0

825 Scholz, C.H. (1968). The frequency-magnitude relation of microfrac- turing in rock and its
826 relation to earthquakes. *Bull. Seismol. Soc. Am.*, *58*, 399–415.

827 Scholz, Christopher H. (2015). On the Stress Dependence of the Earthquake b-value.
828 *Geophysical Research Letters*, *10964*, n/a-n/a. https://doi.org/10.1002/2014GL062863

829 Schorlemmer, D., Wiemer, S., & Wyss, M. (2005). Variations in earthquake-size distribution
830 across different stress regimes. *Nature*, *437*(7058), 539–542.
831 https://doi.org/10.1038/nature04094

832 Shapiro, S. A., Dinske, C., Langenbruch, C., & Wenzel, F. (2010). Seismogenic index and
833 magnitude probability of earthquakes induced during reservoir fluid stimulations. *Leading*
834 *Edge*, *29*(3), 304–309. https://doi.org/10.1190/1.3353727

835 Shelly, D. R., Ellsworth, W. L., & Hill, D. P. (2016). Journal of Geophysical Research : Solid
836 Earth California , earthquake swarm, 1776–1795.
837 https://doi.org/10.1002/2015JB012719.Received

838 Shi, Y., & Bolt, B. (1982). The standart error of the magnitude-frequency b-value. *Bulletin of the*
839 *Seismological Society of America*, *72*(5), 1677–1687. Retrieved from

http://www.bssaonline.org/content/72/5/1677.abstract

Terakawa, T., Miller, S. A., & Deichmann, N. (2012). High fluid pressure and triggered earthquakes in the enhanced geothermal system in Basel, Switzerland. *Journal of Geophysical Research: Solid Earth*, *117*(7), 1–15. https://doi.org/10.1029/2011JB008980

Utsu, T. (1999). Representation and Analysis of the Earthquake Size Distribution: A Historical Review and Some New Approaches. *Pure and Applied Geophysics*, *155*, 509–535. https://doi.org/10.1007/s000240050276

Valley, B., & Evans, K. F. (2009). Stress orientation to 5 km depth in the basement below Basel (Switzerland) from borehole failure analysis. *Swiss Journal of Geosciences*, *102*(3), 467–480. https://doi.org/10.1007/s00015-009-1335-z

Valley, B., & Evans, K. F. (2015). Estimation of the Stress Magnitudes in Basel Enhanced Geothermal System. *World Geothermal Congress 2015*, (April), 12.

Valley, B., & Evans, K. F. (2019). Stress magnitudes in the Basel enhanced geothermal system. *International Journal of Rock Mechanics and Mining Sciences*, *118*(November 2018), 1–20. https://doi.org/10.1016/j.ijrmms.2019.03.008

Waldhauser, F., & Ellsworth, W. L. (2000). A Double-difference Earthquake location algorithm: Method and application to the Northern Hayward Fault, California. *Bulletin of the Seismological Society of America*, *90*(6), 1353–1368. https://doi.org/10.1785/0120000006

Wiemer, S., & Wyss, M. (1997). Mapping the frequency-magnitude distribution in asperities: An improved technique to calculate recurrence times? *Journal of Geophysical Research*, *102*(3), 15115. https://doi.org/10.1029/97JB00726

Yoshida, K., Hasegawa, A., & Yoshida, T. (2016). Temporal variation of frictional strength in an earthquake swarm in NE Japan caused by fluid migration. *Journal of Geophysical Research: Solid Earth*, *121*(8), 5953–5965. https://doi.org/10.1002/2016JB013022

Yoshida, K., Saito, T., Urata, Y., Asano, Y., & Hasegawa, A. (2017). Temporal Changes in Stress Drop, Frictional Strength, and Earthquake Size Distribution in the 2011 Yamagata-Fukushima, NE Japan, Earthquake Swarm, Caused by Fluid Migration. *Journal of Geophysical Research: Solid Earth*, *122*(12), 10,379-10,397. https://doi.org/10.1002/2017JB014334

Ziegler, M., & Evans, K. F. (2020). Comparative study of Basel EGS reservoir faults inferred from analysis of microseismic cluster datasets with fracture zones obtained from well log analysis. *Journal of Structural Geology*, *130*(October 2019), 103923. https://doi.org/10.1016/j.jsg.2019.103923

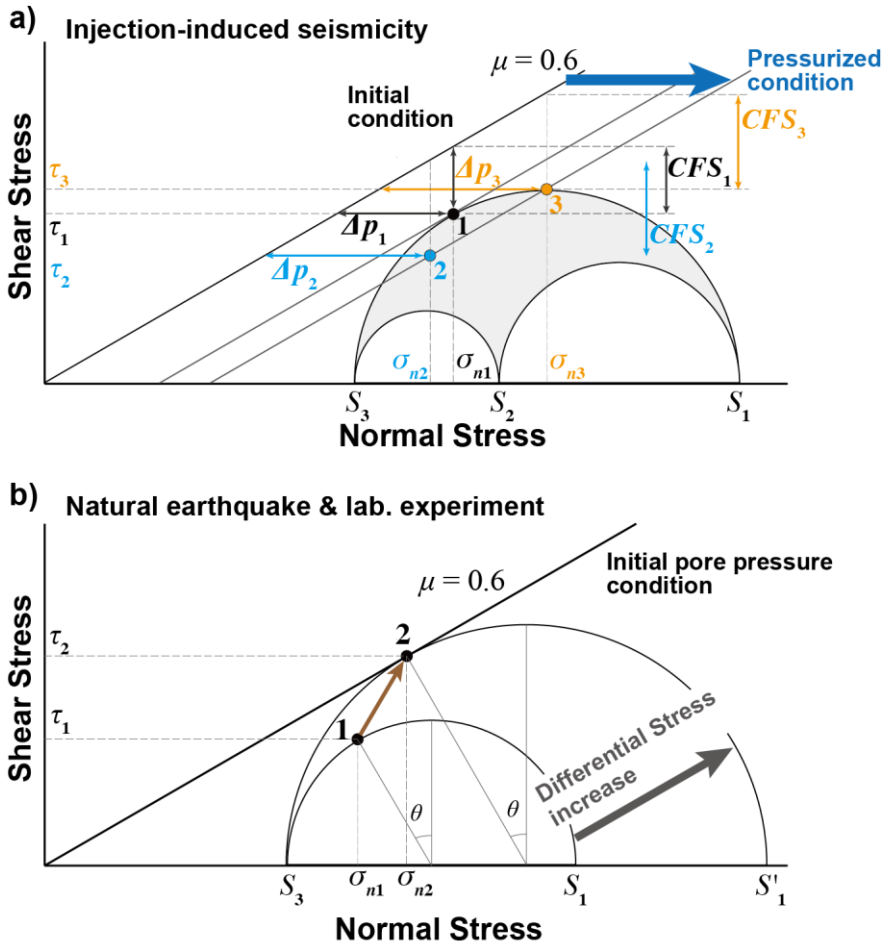

Figure 1. Geomechanical theory described with the Mohr stress circle and the Coulomb failure criterion for **(a)** injection-induced seismicity, and **(b)** natural earthquakes and laboratory experiments. **(a)** A fixed Mohr stress circle, and a Coulomb failure criterion line shifting to the right according to the pore pressure increase. Point 1 plotted on the Mohr stress circle shows the stress state of a well-oriented fault. The shear stress (τ_1) and normal stress (σ_{n1}) along this fault are indicated with broken lines. Pore pressure increase to reactivate this fault is expressed as Δp_1 (the horizontal distance between the initial failure line and point 1). The Coulomb failure stress is expressed as CFS_1 (the vertical distance between the initial failure line and point 1). Point 2 shows the stress state of a non well-oriented fault. Its geomechanical paremeters (τ_2, σ_{n2}, Δp_2, and CFS_2) are shown in the same way as for point 1. **(b)** Small Mohr stress circle showing the stress state before an earthquake (initial stress state) and bigger Mohr stress circle showing the stress state when an earthquake (critical stress state) due to an increase in the maximum principal stress (increasing the differential stress). Points 1 and 2 show the stress state of a well-oriented fault at the initial stress state and the critical stress state.

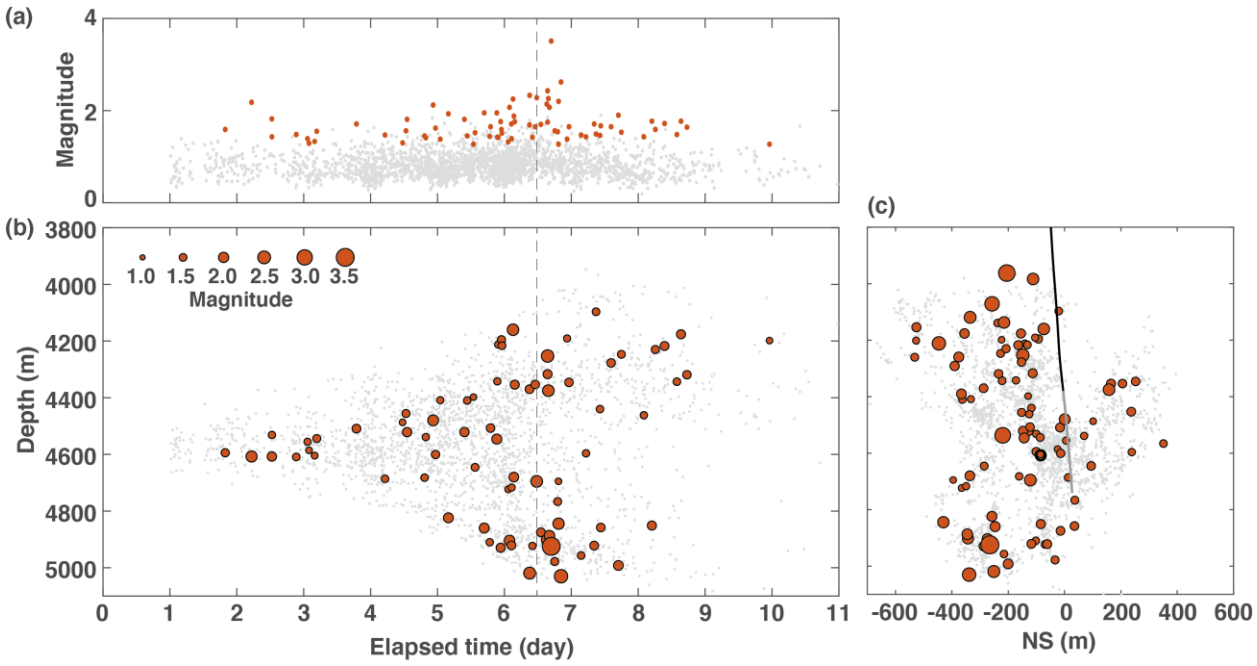

Figure 2. **(a)** Temporal evolution of microseismic magnitudes. The vertical dashed line indicates the time of shut-in. **(b)** Depth migration of microseismic hypocenters. **(c)** Vertical NS cross-section of the reservoir, showing microseismic hypocenters. The black line traces the injection well. In all panels, magnitudes of the events having focal mechanisms estimated by SED are plotted with red circles. The diameters of the circles indicate their event magnitudes.

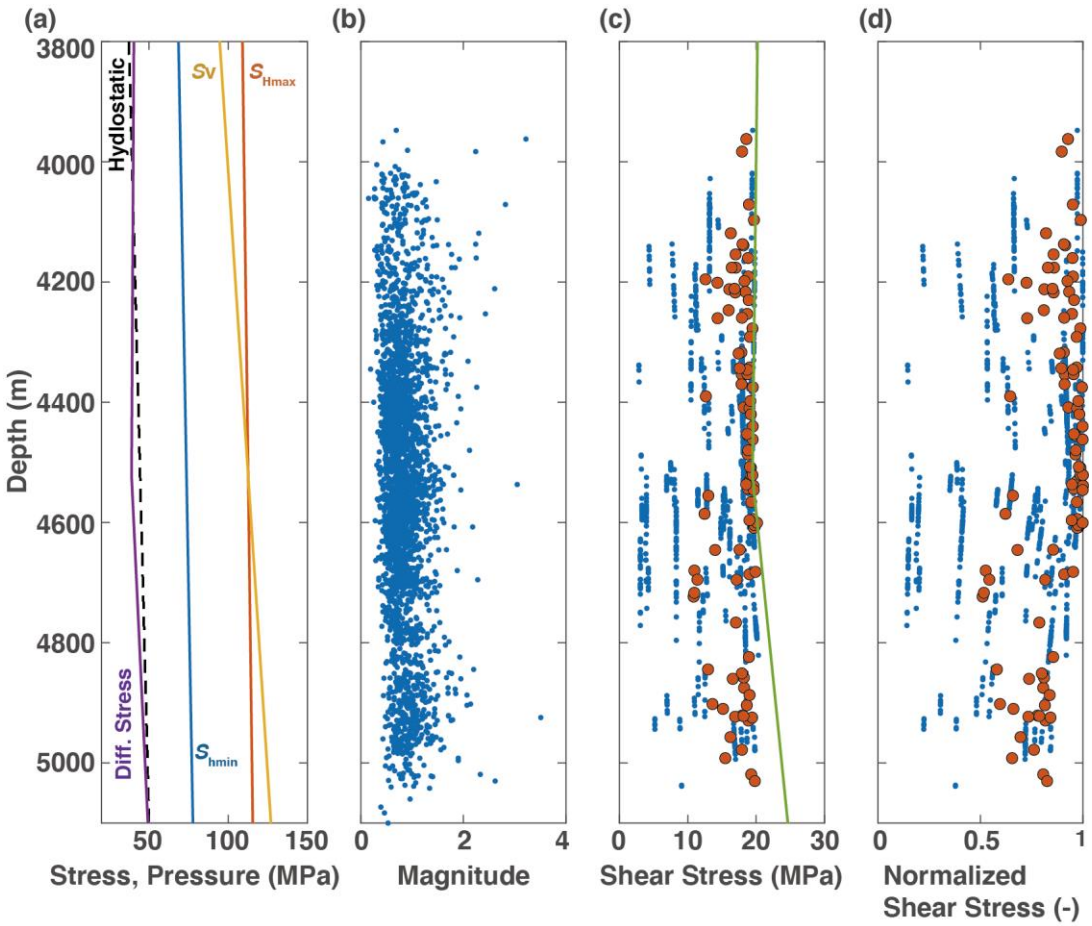

Figure 3. **(a)** Depth profiles of the *in-situ* stresses. The stress regime transitions from a strike-slip stress state to a normal-fault stress state at around 4800 m depth due to the small gradient of S_{Hmax}. The purple line shows the differential stress estimated from the maximum and minimum principal stresses. **(b)** Depth profile of event magnitude M_w. **(c)** Depth profile of shear stress. Orange markers show the shear stress estimated from FPS. Blue markers show the shear stress estimated from cluster analysis. The green line shows the maximum shear stress based on the in-situ stress model. **(d)** Depth profile of normalized shear stress.

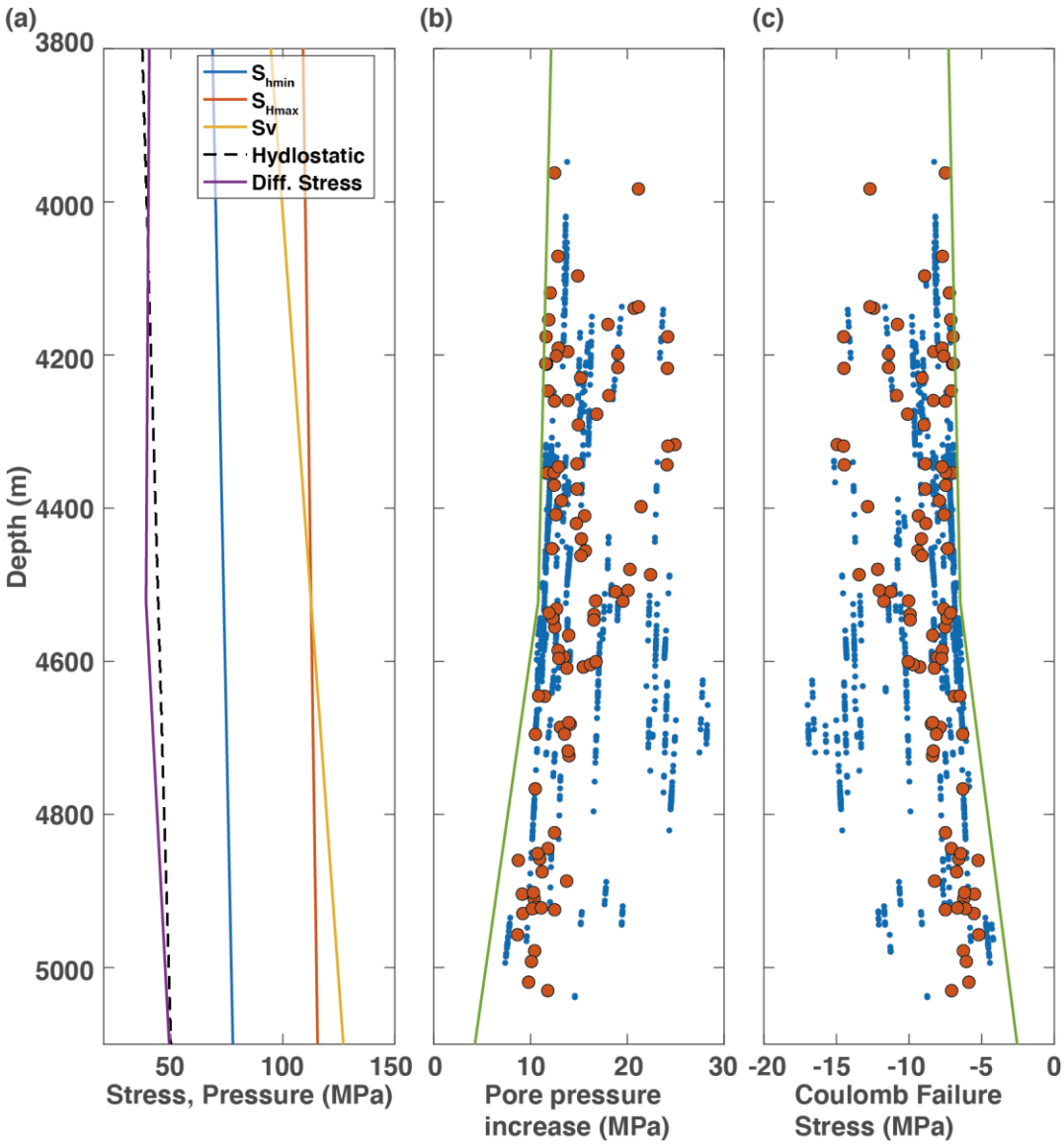

Figure 4. **(a)** Depth profiles of the *in-situ* stresses. **(b)** Depth profiles of pore pressure increase Δp required for fault slip. **(c)** Depth profile of change in Coulomb failure stress (*CFS*) associated with slip. Orange and blue color code is the same as in Figure 3.

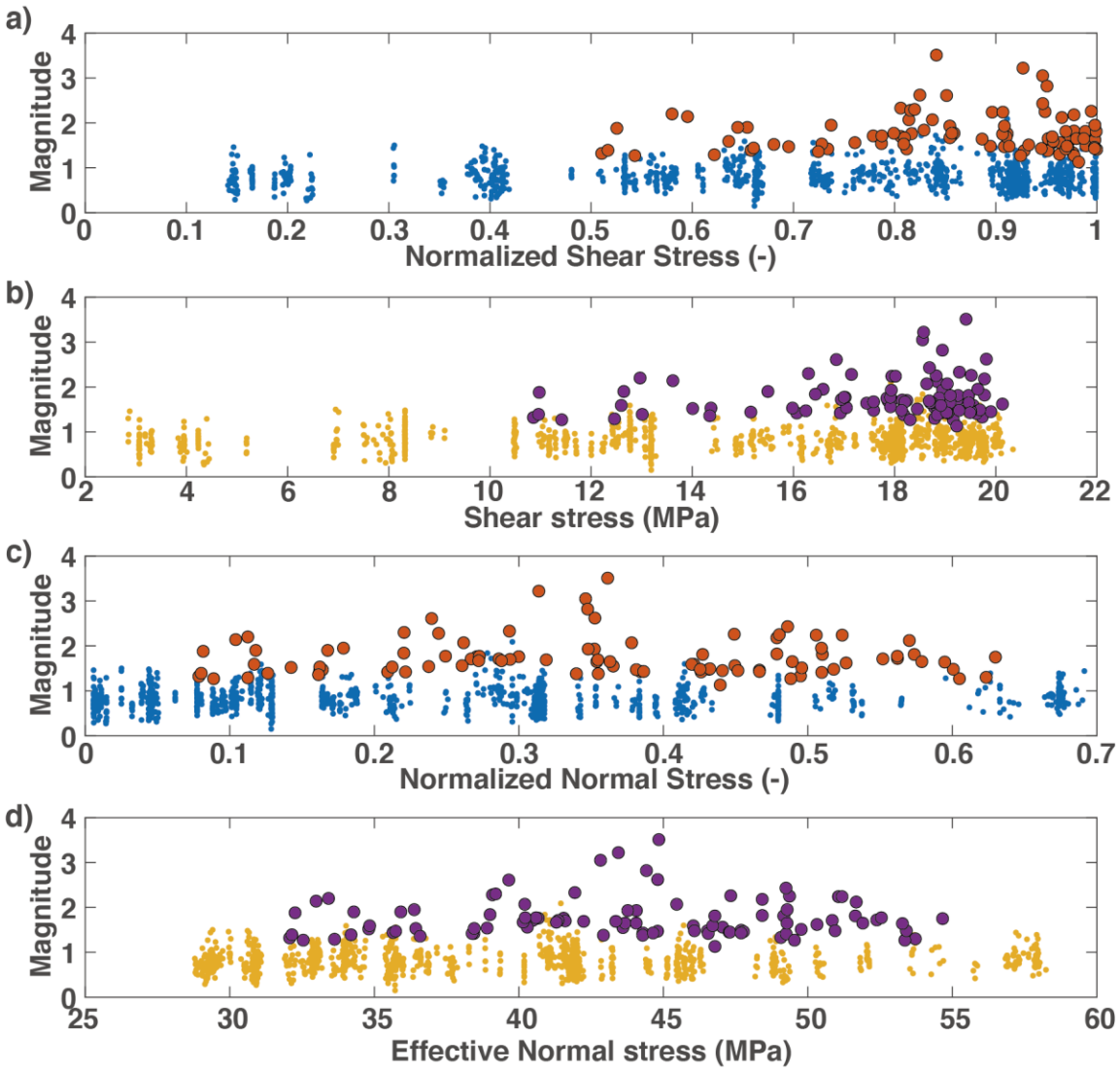

Figure 5. Correlation between the magnitude and shear and normal stress, as well as their normalized forms. The large dots indicate events where FPS was estimate by SED. The small dots show events which were processed using cluster analysis.

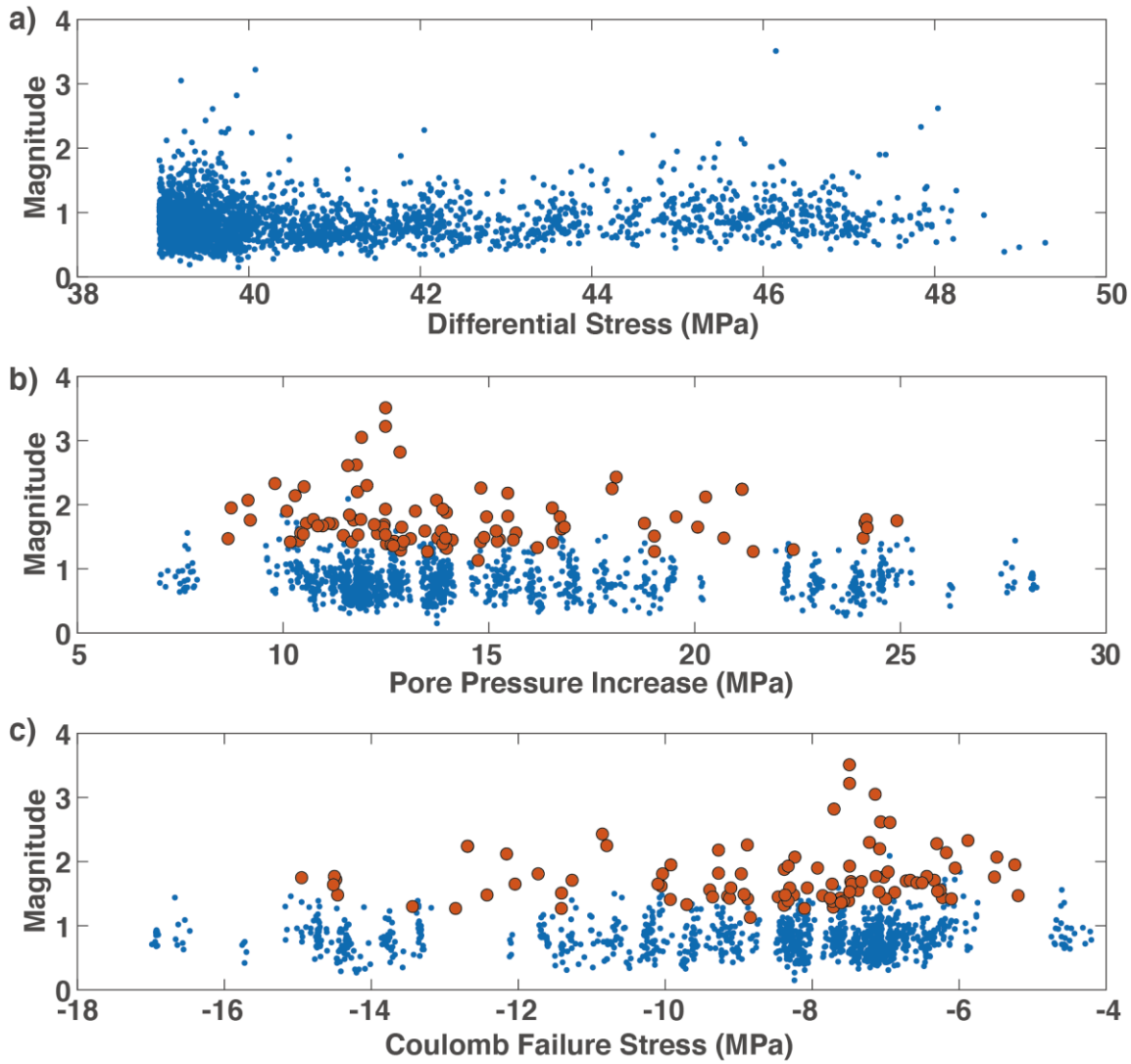

Figure 6. The correlation of magnitude with **(a)** differential stress, **(b)** Δp, and **(c)** ΔCFS. The large markers in **(b)** and **(c)** correspond to the events where FPSs were estimated by SED and the small, blue dots correspond to events with fault orientations estimated by cluster analysis.

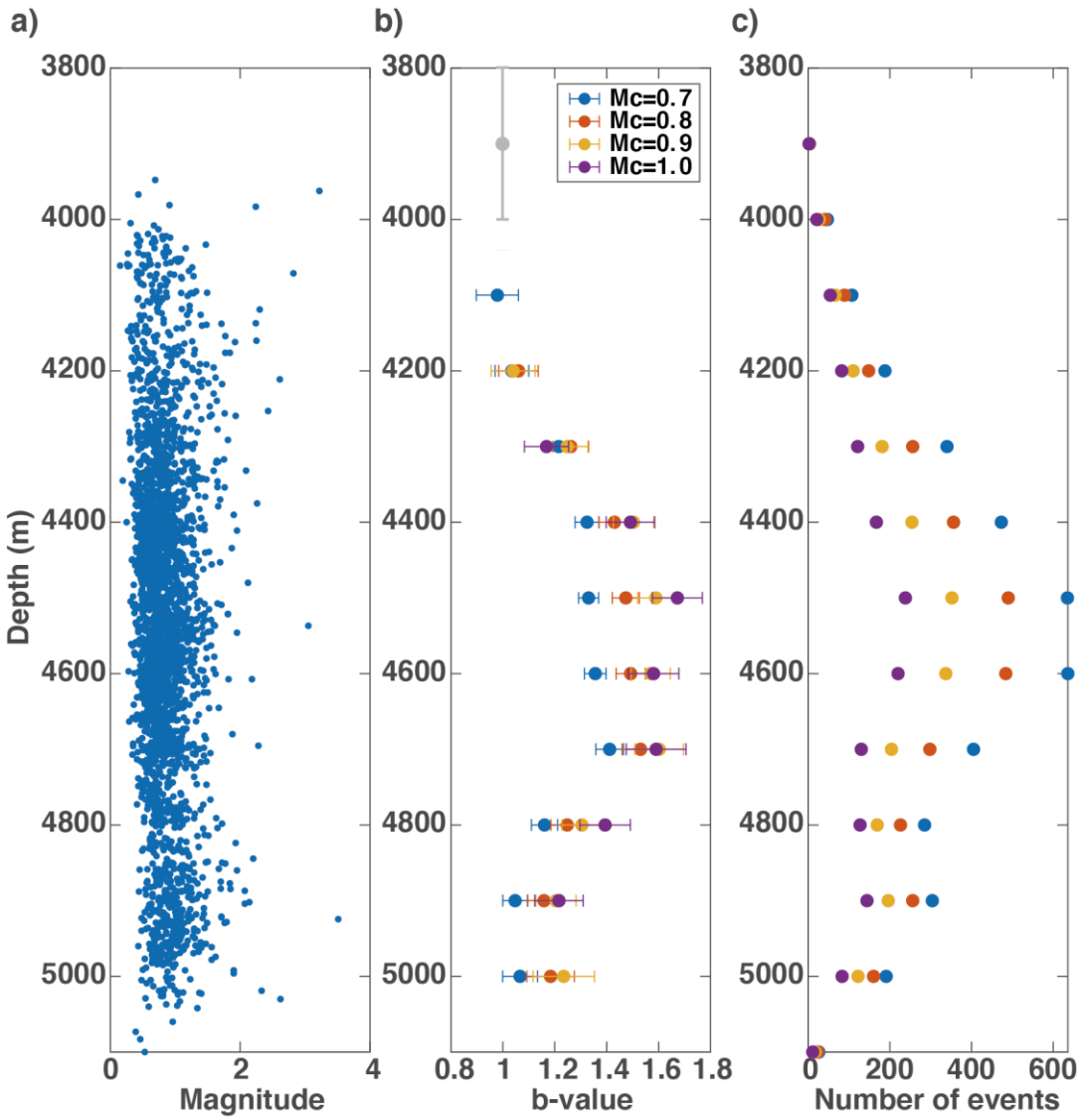

Figure 7. The *b*-value dependency on the event depth. **(a)** Depth profile of magnitude. **(b)** *b*-value variability with depth. The *b*-value is estimated every 100 m with a 200 m bin width, which is indicate by the vertical grey bar. The *b*-values are estimated with four different constant Mc values. **(c)** The number of events used for *b*-value estimation.

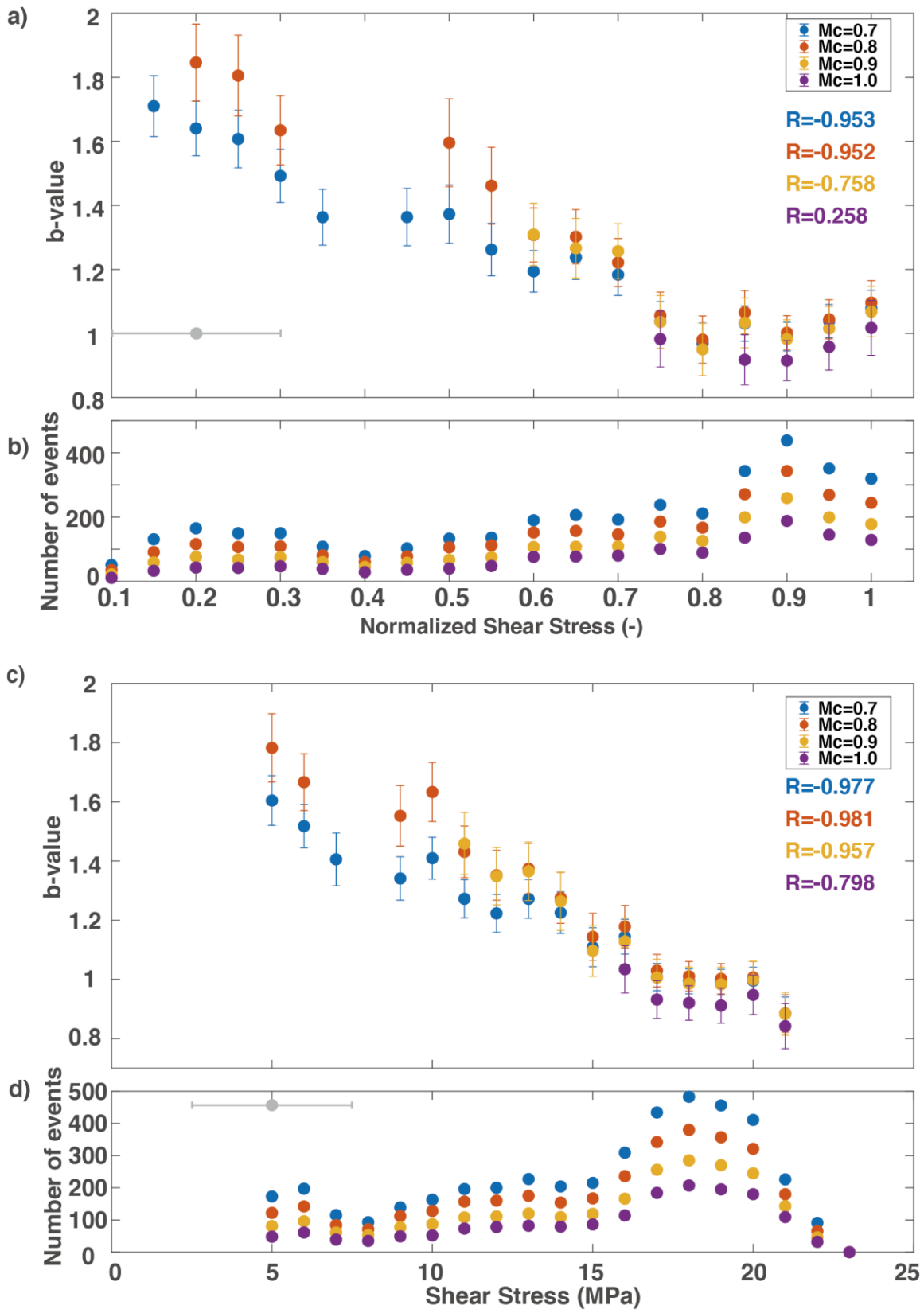

Figure 8. The *b*-value dependency on **(a)** the NSS and **(c)** absolute shear stress. Each color indicates results for different Mcs. R values show the correlation coefficient between *b*-value and The bin length for estimating is 0.2 for NSS and 5 MPa for shear stress as shown with grey horizontal bars. The number of events used to estimate each *b*-value is shown in **(b)** and **(d)**.

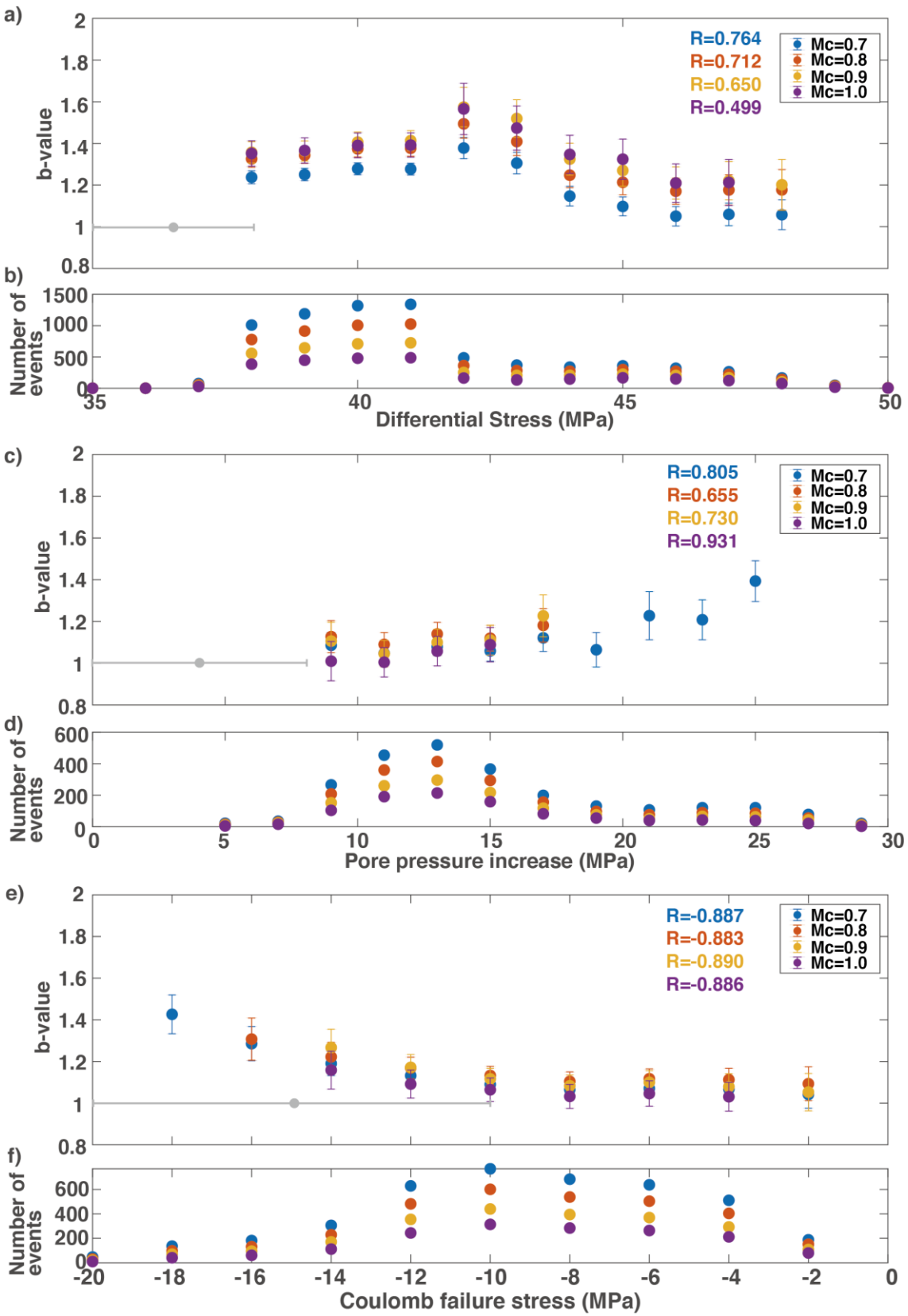

Figure 9. The *b*-value dependency on **(a)** the differential stress, **(c)** pore pressure increase, and **(e)** ΔCFS. The size of the window used to estimate the *b*-value is 4 MPa for differential stress, 8 MPa for Δp, and 10 MPa for CFS, respectively. The lengths of the windows used are depicted by the horizontal grey bars. **(b)**, **(d)**, and **(f)** show the number of events used for *b*-value

estimation for each parameter.

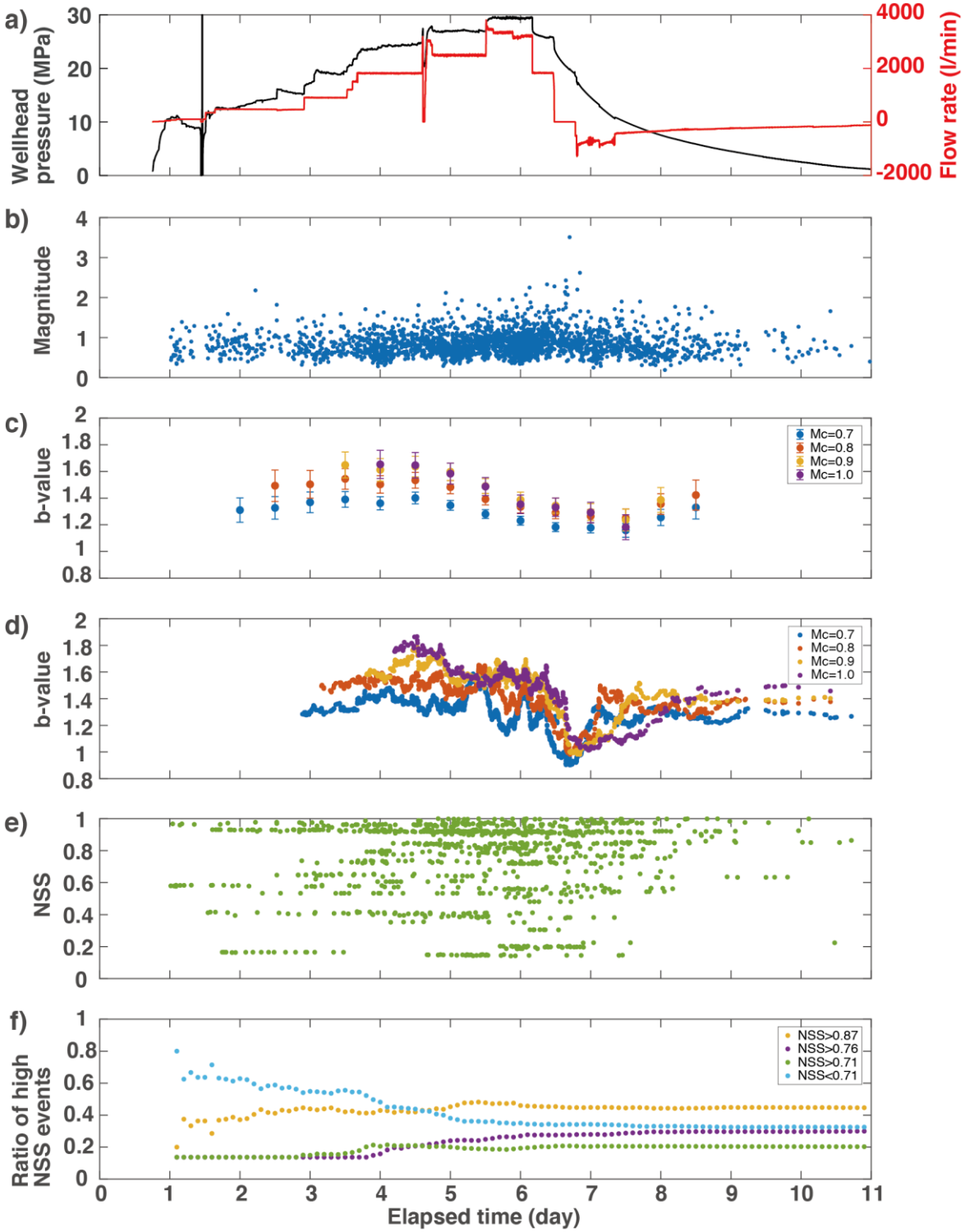

Figure 10. Time series of various parameters. **(a)** Hydraulic record for the injection well. **(b)** Magnitude. **(c)** *b*-value estimated every 0.5 day. **(d)** *b*-value estimated for every event using the 100 preceding events. **(e)** NSS of the events. **(f)** Ratio of the number of events occurring within different NSS ranges.